JOURNAL OF SYNCHROTRON RADIATION
ISSN 1600-5775

Received 21 August 2015
Accepted 11 December 2015

Edited by S. M. Heald, Argonne National Laboratory, USA

Keywords: synchrotron radiography; sample movement; water attenuation coefficient calibration; polymer electrolyte membrane fuel cells; Beer–Lambert law.

Calibrating the X-ray attenuation of liquid water and correcting sample movement artefacts during *in operando* synchrotron X-ray radiographic imaging of polymer electrolyte membrane fuel cells

Nan Ge,[a] Stéphane Chevalier,[a] James Hinebaugh,[a] Ronnie Yip,[a] Jongmin Lee,[a] Patrick Antonacci,[a] Toshikazu Kotaka,[b] Yuichiro Tabuchi[b] and Aimy Bazylak[a]*

[a]Thermofluids for Energy and Advanced Materials Laboratory, Department of Mechanical and Industrial Engineering, University of Toronto, 5 King's College Road, Toronto, Ontario, Canada M5S 3G8, and [b]EV System Laboratory, Research Division 2, Nissan Research Center, Nissan Motor Co. Ltd, 1 Natsushima-cho, Yokosuka-shi, Kanagawa 237-8523, Japan. *Correspondence e-mail: abazylak@mie.utoronto.ca

Synchrotron X-ray radiography, due to its high temporal and spatial resolutions, provides a valuable means for understanding the *in operando* water transport behaviour in polymer electrolyte membrane fuel cells. The purpose of this study is to address the specific artefact of imaging sample movement, which poses a significant challenge to synchrotron-based imaging for fuel cell diagnostics. Specifically, the impact of the micrometer-scale movement of the sample was determined, and a correction methodology was developed. At a photon energy level of 20 keV, a maximum movement of 7.5 μm resulted in a false water thickness of 0.93 cm (9% higher than the maximum amount of water that the experimental apparatus could physically contain). This artefact was corrected by image translations based on the relationship between the false water thickness value and the distance moved by the sample. The implementation of this correction method led to a significant reduction in false water thickness (to ∼0.04 cm). Furthermore, to account for inaccuracies in pixel intensities due to the scattering effect and higher harmonics, a calibration technique was introduced for the liquid water X-ray attenuation coefficient, which was found to be 0.657 ± 0.023 cm^{-1} at 20 keV. The work presented in this paper provides valuable tools for artefact compensation and accuracy improvements for dynamic synchrotron X-ray imaging of fuel cells.

1. Introduction

The polymer electrolyte membrane (PEM) fuel cell is an energy conversion device that provides high energy-efficiency and zero local emissions, and is considered as a promising alternative to the internal combustion engine (Kalidindi *et al.*, 2013; Perng *et al.*, 2014). PEM fuel cells produce electrical power from the electrochemical reaction of hydrogen and oxygen with water and heat as the only by-products. The presence of water in the PEM fuel cell is critical for ensuring membrane hydration, which is required for achieving the necessary levels of ionic conductivity in the membrane (Li *et al.*, 2008). However, water tends to condense and accumulate in the porous gas diffusion layer (GDL), thereby hindering oxygen transport to the reaction site. Effective water management is necessary for achieving optimal performance in the PEM fuel cell.

Due in part to high temporal and spatial resolutions, synchrotron X-ray radiography has been recently developed as a tool for imaging PEM fuel cells and PEM fuel cell materials, particularly to track liquid water transport beha-

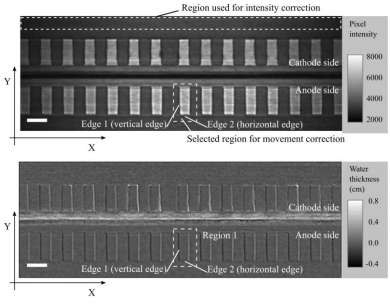

viour (Antonacci *et al.*, 2015, 2016; Büchi *et al.*, 2008; Chevalier *et al.*, 2015; Hartnig & Manke, 2009; Haussmann *et al.*, 2013; Hinebaugh *et al.*, 2012*a*, 2015; Lee *et al.*, 2010; Lee *et al.*, 2013, 2015; Manke *et al.*, 2007). Manke *et al.* (2007) studied the development of liquid water in the GDL with a spatial resolution of 3–7 µm, and observed cathode channel water droplets migrating from the GDL region under the land. Later, Hartnig *et al.* (2009) visualized the water distribution in the through-plane direction and explained that liquid water clusters in the GDL result from repeated Haines jumps and capillary pressure differences in the pores, defined as choke-off effects. Using synchrotron imaging, the roles of GDL structures, such as cracks in the microporous layer (MPL) (Markötter *et al.*, 2013), carbon fibre orientation (Markötter *et al.*, 2015) and perforated holes on the GDLs (Alink *et al.*, 2013; Haussmann *et al.*, 2013; Markötter *et al.*, 2012), in water management were studied. While synchrotron radiography is a powerful tool for visualizing liquid water in the PEM fuel cell, radiation was reported to degrade the fuel cell performance (Eller *et al.*, 2014; Schneider *et al.*, 2010) by damaging the fuel cell materials (Roth *et al.*, 2012) and so must be applied with care.

In synchrotron X-ray imaging, the Beer–Lambert law is commonly employed (Büchi *et al.*, 2008; Lee *et al.*, 2010). This law describes the relationship between the incident beam intensity and the attenuated beam intensity [as shown in Fig. 1(*a*)] based on the attenuation coefficient and the length of the path traversed by the X-ray beam:

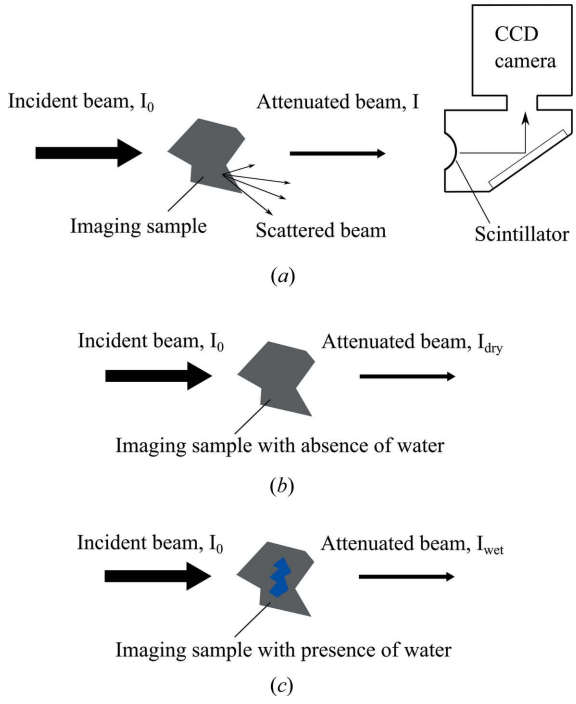

Figure 1
Schematics illustrating: (*a*) the interaction between the incident, parallel X-ray beam and the sample before the CCD measures the detected signal, (*b*) the attenuation process of the imaging sample in the absence of liquid water, and (*c*) the attenuation process of the imaging sample in the presence of liquid water.

$$I = I_0 \exp(-\mu X), \tag{1}$$

where I is the attenuated beam intensity, I_0 is the incident beam intensity, μ is the attenuation coefficient of the material and X is the material thickness along the beam direction (Swinehart, 1962). Lee *et al.* (2010) presented an image normalization technique, which was derived from (1), to quantify the water thickness in the through-plane direction of the GDL. This technique requires a reference image in the absence of liquid water, termed *dry-state image* in this work. This dry-state image was needed in order to determine the water content in the image that contained liquid water, termed the *wet-state image* in this work, using the following equation:

$$X_w = (1/\mu_w) \ln\left(I_{dry}/I_{wet}\right), \tag{2}$$

where X_w is the cumulative water thickness along the X-ray path, and μ_w is the attenuation coefficient of liquid water, which is a function of the photon energy level. I_{dry} is the pixel intensity of the reference dry-state image [as shown in Fig. 1(*b*)], and I_{wet} is the pixel intensity of the target wet-state image [as shown in Fig. 1(*c*)]. By using (2), Hinebaugh *et al.* (2012*b*) developed an image-processing routine to quantify liquid water with the goal of increasing the accuracy of the measured liquid water thickness by compensating for vertical oscillation of the beam position.

While synchrotron radiography has already proven to be a powerful tool for visualizing PEM fuel cells, special attention should be made during the stages of image processing and analysis in order to obtain highly accurate results. A reference value for the attenuation coefficient has been published by the National Institute of Standards and Technology (NIST) (Hubbell & Seltzer, 2004); however, in equations (1) and (2) the attenuation coefficient is a direct function of the material and photon energy level. The liquid water content calculation is highly dependent on the attenuation coefficient of liquid water, yet this attenuation coefficient is not typically calibrated (or reported to be calibrated) in the literature.

Directly applying the reference attenuation coefficient (from NIST) can result in inaccurate image interpretation if one experiences scattering effects or if the incident beam contains harmonic frequencies in addition to the intended frequency. The scattering effect is the process in which a portion of incident photons are redirected from their original path by the sample material (Hendee *et al.*, 1977), as illustrated in Fig. 1(*a*). The scatter angle, which describes the travel direction of a scattered photon with respect to the incident beam direction, is unpredictable (Sprawls, 1977). Hence, in practice, the scattered photons can be unintentionally measured at the scintillator, unfortunately contributing to the pixel intensity of the collected image.

Higher harmonics contamination is the phenomenon whereby a portion of the incident photons from the double-crystal monochromator exhibit undesired higher energy levels, which are integer multiples of the fundamental (prescribed) energy level (Chapman *et al.*, 1992; Hrdý *et al.*, 2011). The attenuation coefficient of the sample is lower for the high-energy photon beam, compared with that for the fundamental

energy level. By applying the reference attenuation coefficient of the fundamental energy level, an error is introduced when quantifying the liquid water *via* the Beer–Lambert law. Therefore, an experimentally calibrated attenuation coefficient is vitally needed in order to account for scattering and higher harmonic effects.

Sample movement at the micrometer scale during *in operando* imaging can also be a significant source of image artefacts. The image normalization technique based on equation (2) was established upon the condition that the sample does not move during the imaging process. The normalization calculation relies on the pixel intensity change to be solely caused by the presence of liquid water. However, if the sample moves during the imaging process, false water thicknesses will be observed. For example, as shown in Fig. 2, a normalized image processed solely using the technique by Hinebaugh *et al.* (2012*b*) results in false water thicknesses including negative and positive values at the anode channel edges (where liquid water was not expected based on the experimental conditions used). Movement artefacts decrease the accuracy of liquid water measurements and, without properly addressing sample movement, synchrotron radiography-based imaging could be rendered unusable.

In this work we present a method for calibrating the liquid water attenuation coefficient and the details of the image-processing technique used to account for sample movement during *in situ* PEM fuel cell investigations of liquid water transport. The image-processing techniques presented here can be used for future synchrotron X-ray based imaging of the PEM fuel cell for enhancing the accuracy of liquid water quantifications.

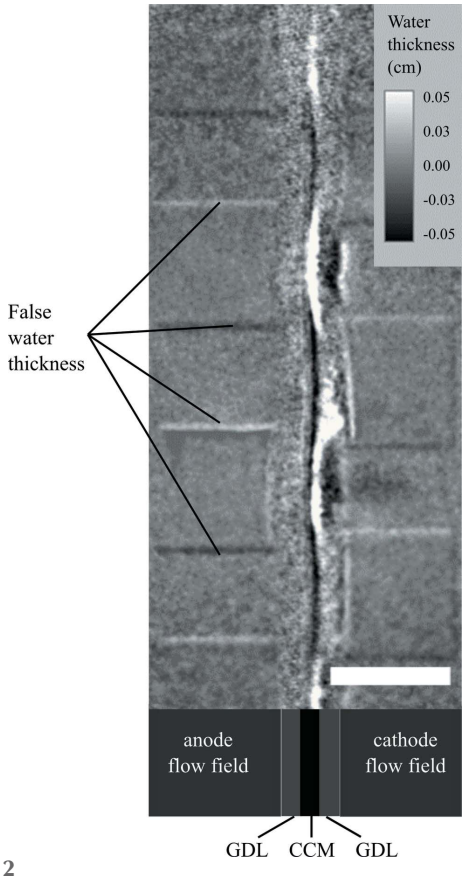

Figure 2
Example processed image obtained from synchrotron X-ray radiography of an operating PEM fuel cell before the movement correction was applied. The appearance of false water thicknesses is highlighted and the length bar is 0.5 mm.

2. Methodology

2.1. Fuel cell hardware and control

The PEM fuel cell considered in this study consisted of cathode and anode flow fields, GDLs and a catalyst-coated membrane electrode assembly (CCM) as shown in the radiograph in Fig. 3. The channels of the flow fields had a width of 0.2 mm and a depth of 0.5 mm. The GDL is herein defined as the combined carbon paper substrate and MPL. The TGP-H-60 (Toray Industries) carbon paper substrate was used for the *in operando* experiment described in this work. The GDL was compressed to 85% of its original thickness using polyethylene naphthalate (PEN) spacers. The active area had a width of 0.80 cm and a length of 0.85 cm, where the length coincided with the distance traversed by the X-ray beam.

The PEM fuel cell was mounted to the sample stage using four stainless steel bolts and was controlled using a Scribner 850e fuel cell test station (Scribner Associates Inc.). During the experiments, gaseous hydrogen and air were set to a relative humidity (RH) of 100% and a temperature of 60°C at both the cathode and anode. The inlet flow rate was set to 1 L min^{-1} at a pressure of 2 atm (absolute). The operating temperature of the fuel cell was set to 60°C and controlled with a water-cooling system (Fig. 3). The low operating temperature and high reactant RH were chosen to promote the accumulation of liquid water in order to impose the saturated conditions that are unfavourable in practical applications. In addition, high current density operation was constrained to a short period of time in order to avoid cathode flooding and the back diffusion of water to the anode. As a result, liquid water transport was restricted to the cathode side during the experiments.

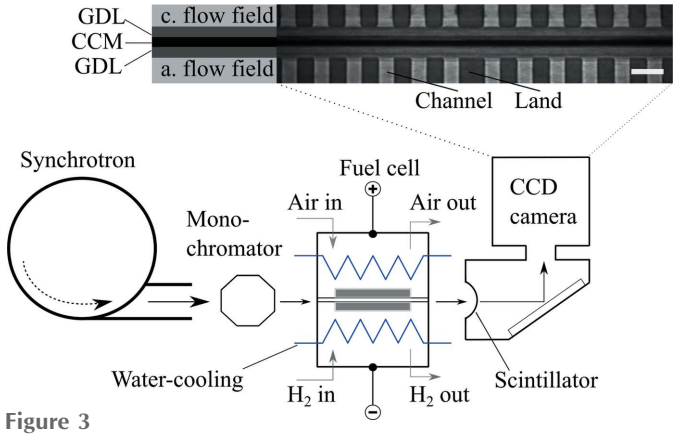

Figure 3
Schematic showing the orientation of the fuel cell apparatus and the incident beam during synchrotron X-ray radiographic imaging. The top inset illustrates fuel cell components in the obtained radiograph and the length bar is 0.4 mm.

2.2. Synchrotron imaging

The images presented in this work were obtained from *in operando* PEM fuel cell imaging work conducted at the Biomedical Imaging and Therapy Bending Magnet (BMIT-BM) 05B1-1 beamline at the Canadian Light Source synchrotron facility in Saskatoon, Canada (Wysokinski *et al.*, 2007). The photon energy level of the beam was set to 20 keV. A Hamamatsu ORCAII-ERG camera (Hamamatsu Photonics KK) was used, and in order to obtain a high signal-to-noise ratio the camera was set to the high-precision readout mode. At this setting the dynamic range of the charge-coupled device (CCD) camera was 4625:1, based on a readout noise of 4 electrons and a full well capacity (maximum amount of charge that each pixel can hold before saturating) of 18500 electrons. A 14-bit analog-to-digital converter was used, which resulted in a pixel intensity range of 0–16383. The exposure time was set to 1.7 s, and every image was obtained from averaging four sequential frames. A buffer time of 1.5 s was applied during image acquisition to facilitate camera read-out and to ensure a constant frame rate. The resulting temporal resolution (time duration between two consecutive images) was 8.3 s. A pixel resolution of 4.4 μm pixel^{-1} was obtained.

2.3. Experimental protocol

The primary purpose of using synchrotron radiography with *in situ* PEM fuel cell diagnostics was to accurately measure the liquid water content in the cathode GDL, specifically the water thickness (or equivalent saturation) distribution. The water thickness is defined as the summation of liquid water content accumulated in the in-plane direction traversed by the X-ray beam. In this study, the term *normalized image* refers to an image obtained using equation (2), and the water thickness corresponds to the pixel brightness in the normalized image.

During the fuel cell experiment, three sets of images were captured in the following sequence: (1) ten dark-field images, (2) five dry-state images, and (3) wet-state images (of the *in operando* fuel cell experiment). In this study the term *image stack* refers to the sequence of images of the *dry state* and *wet state* collected *in situ*. The first dry-state image occurred at time $t = 0$, and the location of the fuel cell in this image is the *reference location* for the image stack. An image number (frame number), n, depending on the collection time was assigned to each image in an image stack. For example, at time $t = 0$ the first dry-state image was prescribed an image number $n = 1$.

The dark-field image was obtained without the application of the incident X-ray beam, and the purpose of the dark-field image was to measure the background noise of the camera. The pixel intensities in the dark-field images ranged from ∼2100 to ∼2300. Any non-zero pixel intensities detected in the dark-field image were the result of the dark-current noise generated from the electron thermal excitation in the CCD camera (Widenhorn *et al.*, 2002). Minimizing dark-current noise was ideal for obtaining accurate water thickness measurements.

The dry-state images were obtained at open circuit voltage (OCV) with the incident X-ray beam. During OCV conditions, the membrane was humidified with fully moisturized reactant gases (100% RH). Steady-state OCV conditions were used to ensure that any pixel intensity changes (especially near the interfaces of CCM and GDLs) were not caused by membrane swelling due to changes in humidity (Hwang *et al.*, 2013).

The wet-state images were collected during cell operation in the presence of electrochemically produced water. The pixel intensity of the cathode region in the wet-state images is lower than that in the dry-state images due to the attenuation of the X-rays by liquid water. During operation, the fuel cell was set to current densities typically ranging from 0 to 3.0 A cm^{-2}. The fuel cell was held at each current density for at least 5 min in order to reach steady state. Hence, the duration of each *in situ* fuel cell experiment was approximately 1–2 h (a time period over which 450–900 images were obtained).

2.4. Attenuation coefficient calibration

To account for the unique scattering effect and higher harmonics of the beam (in comparison with NIST conditions), a calibration technique was created to experimentally determine the attenuation coefficient for liquid water at the beamline. Because of scattering and higher harmonics (discussed in §1), the measured intensity at the scintillator was higher than the attenuated intensity. Hence, we anticipated that our attenuation coefficient would be lower than the NIST reference value (0.810 cm^{-1} at 20 keV; Hubbell & Seltzer, 2004).

A custom-made calibration device containing a single liquid water reservoir was developed, as shown in Fig. 4(*a*). The device held six known thicknesses of water (X_{water}) in distinct regions (R_1, R_2, ..., R_6) ranging from 0 to 1.6 cm (Table 1). The expected accuracy level of these lengths was ±0.02 cm, which accounts for machining and assembly tolerances. This device was composed of polycarbonate (PC), which was chosen specifically to simulate the scattering and attenuation effects due to the higher harmonics that would occur during *in operando* fuel cell imaging. The material attenuation coefficient of the PC (∼0.620 cm^{-1} at 20 keV; Hubbell & Seltzer, 2004) was comparable with the carbon-based GDL (0.995 cm^{-1} at 20 keV; Hubbell & Seltzer, 2004) and the PEN spacer [∼0.747 cm^{-1} at 20 keV, estimated based on information provided by the Center for X-ray Optics (2009) and NIST (Hubbell & Seltzer, 2004)]. A critical feature of this device is the constant solid material thickness [X_{PC} on Fig. 4(*a*)] adjacent to each prescribed water thickness region. Thus, while the liquid water induced attenuation should change with varying X_{water}, the beam attenuation induced by the solid material of the device itself should remain constant.

During the calibration experiment, a sequence of images consisting of ten dry-state images, ten dark-field images and ten wet-state images were obtained. The dry-state images were collected when the water compartment of the calibration device was free of water; the wet-state images for this device were collected when the water compartment was filled with

Table 1
Water thickness for each of the regions, R, for the calibration device shown in Fig. 4(*a*).

Region name	Water thickness (cm)
R_1	0
R_2	0.33
R_3	0.63
R_4	0.96
R_5	1.27
R_6	1.60

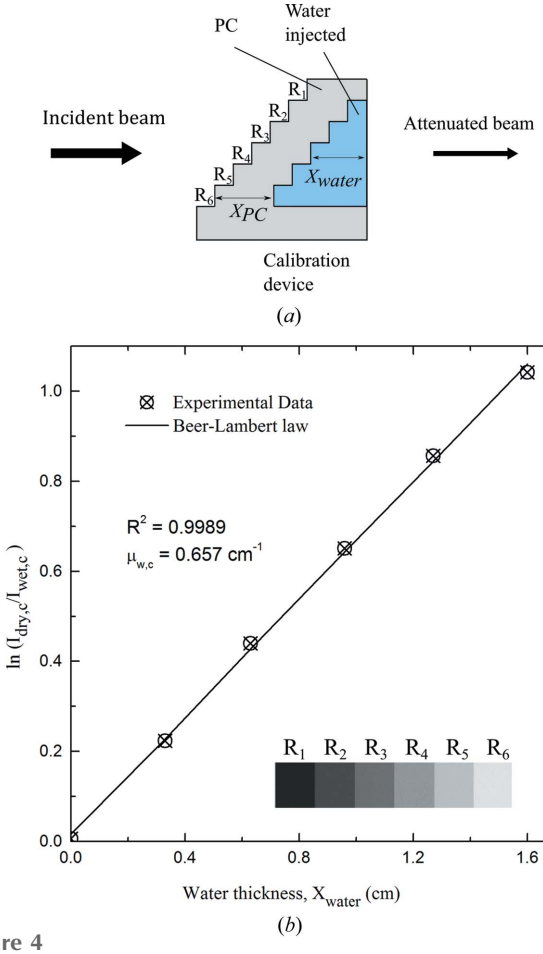

Figure 4
Illustration of the liquid water attenuation coefficient calibration: (*a*) top view of the calibration device; (*b*) determination of the attenuation coefficient; the inset illustrates the processed image of $\ln(I_{\rm dry,c}/I_{\rm wet,c})$ for each region.

water. The calibration experiment was conducted over a period of 5 min.

2.5. Image processing

This section includes the explanation of the four steps that constitute the image-processing methodology for obtaining water thickness distributions: (1) dark-current noise elimination, (2) water attenuation coefficient measurement, (3) beam intensity correction, and (4) sample movement correction. In particular, the description of steps (2) and (4) are the most recent developments in our group's image-processing methodology. The purpose of advancing our image-processing methodology was to increase the accuracy of the measured water content by removing the effects of CCD camera noise, scattering, higher harmonics, intensity change of the synchrotron beam, and sample movement.

2.5.1. Dark-current noise elimination. The dark-current noise signal is pixel-dependent and fluctuates. Therefore, the ten dark-field images were averaged in order to quantify the average noise at each pixel. Then, the average dark-field image was subtracted from each dry-state and wet-state image using the following equation (Widenhorn *et al.*, 2002):

$$I_{\rm nf} = I_{\rm raw} - I_{\rm d} \qquad (3)$$

where $I_{\rm nf}$ is the *noise-free* pixel intensity, $I_{\rm raw}$ is the measured pixel intensity of the raw image, and $I_{\rm d}$ is the averaged pixel noise intensity. The *noise-free* image obtained from equation (3) is our best estimation for the ground truth images. This noise elimination process was performed for both image stacks collected from the fuel cell experiment and the calibration experiment.

2.5.2. Water attenuation coefficient measurement. The noise-free dry-state and wet-state images from the calibration experiment were used to determine the attenuation coefficient of liquid water. Based on equation (2), the attenuation coefficient can be determined using linear regression. Hence, the water thickness of each region in the calibration device (in Table 1) was obtained based on prior knowledge of the device dimensions, and the natural logarithm of the ratio of the dry-state intensity to the wet-state intensity, *i.e.* $\ln(I_{\rm dry}/I_{\rm wet})$, for each region was determined based on the noise-free images from the calibration experiment.

Each noise-free dry-state and wet-state image was obtained from an average of ten sequential images. The pixel intensity in this dry-state image was denoted by $I_{\rm dry,c}$, and the pixel intensity in the wet-state image was denoted by $I_{\rm wet,c}$. The subscript 'c' indicates that a calibration image was used. Accordingly, $\ln(I_{\rm dry,c}/I_{\rm wet,c})$ was calculated for each region [shown in Fig. 4(*b*)].

The expression $\ln(I_{\rm dry,c}/I_{\rm wet,c})$ as a function of the water thickness produced a linear relationship [shown in Fig. 4(*b*)], the slope of which was the water attenuation coefficient ($\mu_{\rm w,c} = 0.657 \pm 0.023$ cm^{-1}, using the least-squares regression method). The value has a confidence interval of 90%, calculated using the Student's t distribution (Neville & Kennedy, 1964).

2.5.3. Beam intensity correction. The incident beam intensity at the Canadian Light Source decreased with time due to the current loss of the electron beam in the storage ring (Hinebaugh *et al.*, 2012*b*). In this case, even over short time periods this intensity change is approximately linear, as verified by monitoring the beam current. The duration of an *in situ* fuel cell experiment was typically more than 1 h; therefore, the beam intensity dependence on time was an important factor in our analysis. However, a critical assumption of equation (2) is that the change in pixel intensity occurs strictly due to the

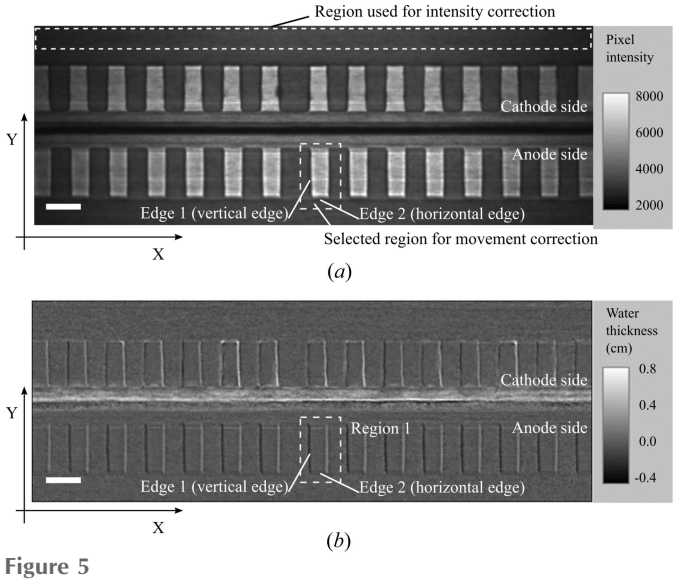

Figure 5
Example synchrotron X-ray radiographic images of an operating PEM fuel cell: (*a*) raw wet-state image, and (*b*) normalized image prior to movement correction. The length bar is 0.4 mm.

attenuation of liquid water. Therefore, a linear intensity correction was required.

For each image, a beam intensity correction factor was first obtained, and then this factor was applied to all the pixels of the corresponding image. It was important that the region selected for determining the correction factor did not contain liquid water for the duration of the experiment, so that we could strictly attribute the intensity change to a loss in beam intensity. The correction factor was calculated from our analysis of the top side of the cathode bipolar plate [shown in Fig. 5(*a*)]. The correction factor was determined as follows:

$$f^n = 1 - \left(\frac{n-1}{N-1}\right)\frac{\overline{I}_1 - \overline{I}_{\rm end}}{\overline{I}_1}, \qquad (4)$$

where n is the image number, $\overline{I}_1$ and $\overline{I}_{\rm end}$ are the mean intensity of the selected region in the first and last noise-free images of the stack, and N is the number of images in the stack. The corrected pixel intensity, $I^n_{\rm cr}$, was determined using the factor, f^n, and the noise-free pixel intensity, $I^n_{\rm nf}$:

$$I^n_{\rm cr} = (1/f^n)\, I^n_{\rm nf}. \qquad (5)$$

2.5.4. Sample movement correction. During the *in situ* experiment, sample movement occurred. The mechanical vibrations from the operating fuel cell test station and the water-cooling system may have contributed to the change in position of the mounting bolts. In this section, the cause of false water thickness due to sample movement is explained and the steps used for image correction are presented.

Cause of false water thickness. Fig. 5(*b*) shows an image of the fuel cell during operation that was normalized through equation (2) using the first dry-state image, *i.e.* $I^1_{\rm cr}$, and the wet-state image of Fig. 5(*a*). Region 1 highlights the selected anode flow channel used for determining the appropriate movement correction, and this region is also noted in Fig. 5(*a*). Region 1 is located in the centre region of this image where the beam intensity is the highest, helping to ensure that the artefact value of the false water thickness was measured with the optimal degree of precision. Since liquid water was not expected in Region 1 (due to the imposed operating conditions), the pixel intensities in Region 1 are expected to be 0. However, in Fig. 5(*b*) a thin band of negative values and a bright band of positive values can be observed at the two vertical channel edges of Region 1 (left and right, respectively). These false water thickness values were attributed to sample movement.

Fig. 6 provides an illustration of how sample movement leads to the determination of false water thicknesses. We define x_0 as the horizontal reference location of the dry-state image. During the experiment, the fuel cell moved to the left (in the negative x direction), causing a phenomenon described as pixel material mismatch, whereby the location of a pixel in one image represents a different position of the sample in a subsequently obtained image. Hence, as a result of equation (2), false water thicknesses at the channel edges were observed in the normalized image. The value of false water thickness was influenced by the distance moved by the sample in the wet-state image with respect to the reference location. In Fig. 6, a line across the vertical channel edge with a height of a single pixel (marked on the inset of the figure) was selected to explain this relationship. The pixel intensities of this line in both the dry-state and the wet-state images were presented. The pixel intensity has a value of ~1700 at the land, increasing to a value of ~3000 at the channel where the beam is attenuated by less material. The pixel intensity of the region between the land and the channel has a gradual and close-to-linear change. This region is termed the *edge transition region* in this work, and the width of the edge transition

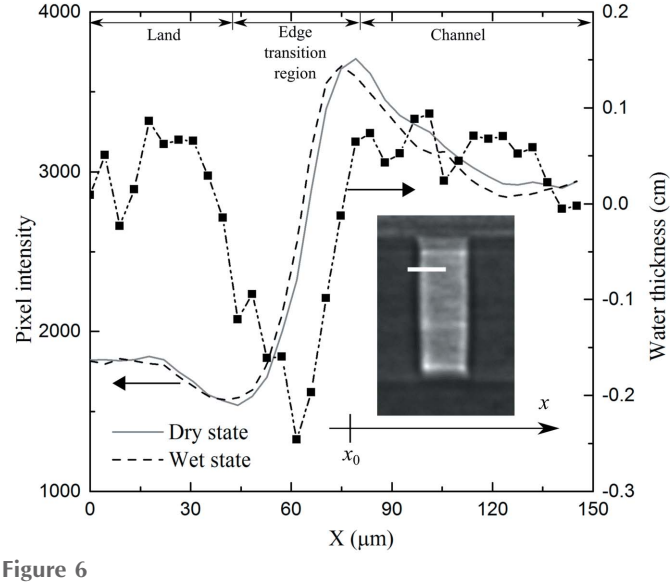

Figure 6
Calculated false water thickness caused by the sample movement. Pixel intensities in the dry-state and moved wet-state images and the calculated water thickness were taken over the white line in the inset.

region is dependent on the angle (yaw) alignment of the fuel cell with the X-ray beam and the spatial resolution available at the beamline facilities. In this example, the movement of ~2 μm caused a maximum false water thickness of −0.25 cm. Increasing distances moved by the sample correspond to larger intensity differences at the edge transition region. Therefore, based on equation (2), the artefact value of false water thickness corresponds to the magnitude of the distance moved.

Artefact calibration. Motivated by the cause of the false water thickness, a two-step correction method was developed. We translated an image over a large range of distances moved to produce all the possible false water thickness values. By image translation, the sample movement was artificially simulated in order to determine the relationship between the false water thickness and the distance moved.

The selected anode channel region as shown in Fig. 5(*a*) from the first image, *i.e.* $n = 1$, was used to calibrate the movement. To simulate the horizontal sample movement during the experiment, this region was translated in the horizontal direction within a ±2 pixel range in increments of 0.01 pixels. As a result, 400 translated images were produced, and each image corresponded to a prescribed distance moved. To determine the false water thickness associated with each distance moved, the translated images were normalized to the original untranslated image using equation (2). For each of the 400 normalized images (each of which corresponds to a distinct distance moved), the false water thickness with the largest absolute value along Edge 1 (Fig. 5*b*) was assigned as the corresponding negative water thickness.

To obtain the relationship between the false water thickness and vertical distance moved, the selected anode channel region [shown in Fig. 5(*a*)] was translated in the vertical direction within a ±2 pixel range in increments of 0.01 pixels. The same procedure described above for calibrating the horizontal distance movement was also employed here for calibrating the vertical distance moved. For each of the 400 normalized images (each of which corresponded to a distinct vertical distance moved), the false water thickness with the largest absolute value along Edge 2 (Fig. 5*b*) was assigned as the corresponding false water thickness. The calibration curves for horizontal and vertical distances moved are shown in Figs. 7(*a*) and 7(*b*), respectively.

Calculation of distances moved and image translation. Based on the calibration relationships presented in Fig. 7, the distances moved within each image from the image stack (of the *in situ* fuel cell experiment) were determined using the respective normalized image prior to the application of the movement correction. Each *in situ* image was normalized to the first dry-state image using equation (2). The horizontal movement for each image distance was determined by correlating the false water thickness along Edge 1 [reference location shown in Fig. 5(*b*)] to the corresponding horizontal distance moved in the calibration curve (Fig. 7*a*). For example, the largest measured false water thickness relating to a horizontal movement was −0.93 cm, and, according to the calibration curve (Fig. 7*a*), the sample moved 1.7 pixels (or 7.5 μm) to the left of the reference location during the experiment. The vertical movement was also determined by applying the same analysis to Edge 2.

After the horizontal and vertical sample movements were determined, each original raw image was translated to the reference location, which was the position of the fuel cell at time $t = 0$ (as described in §2.3). After this translation, the corrected water thicknesses could be determined. The five corrected dry-state images were combined and averaged to produce a single dry-state image used to account for the fluctuation and instabilities of the beam. Each subsequent wet-state image (raw and corrected for sample movement) was then normalized to this averaged dry-state image using equation (2). The final corrected water thickness values were

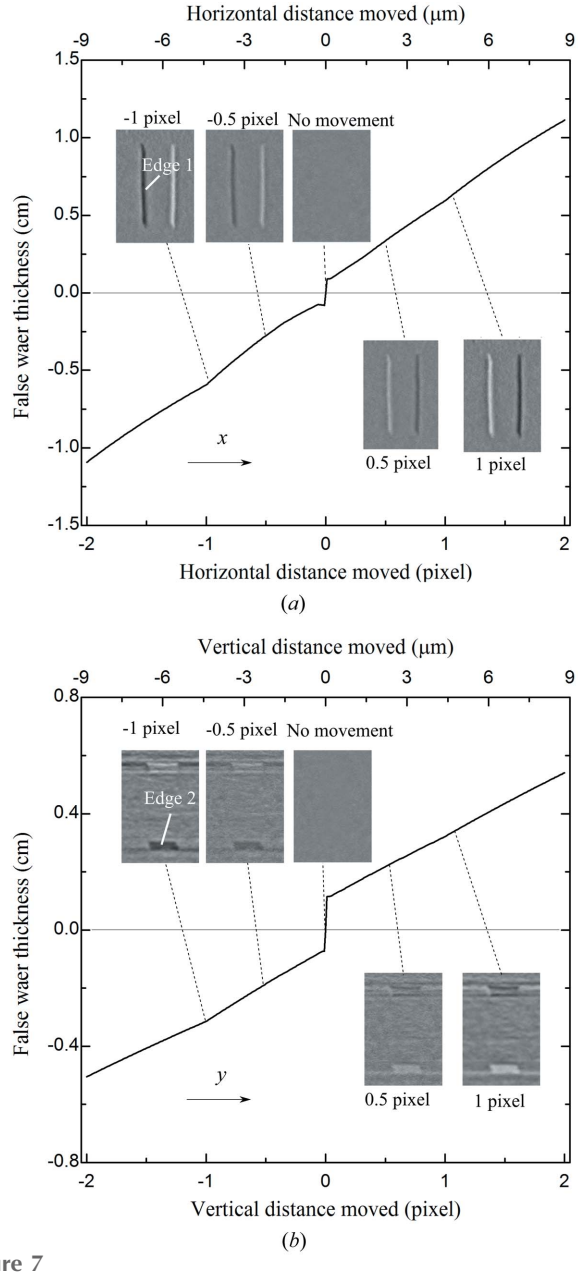

Figure 7
Calibration curves relating false water thicknesses to distance moved due to sample movement: (*a*) horizontal direction and (*b*) vertical direction.

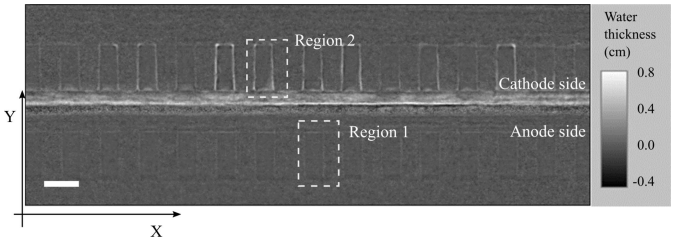

Figure 8
Example synchrotron X-ray radiograph after the movement correction has been applied. The two regions highlighted were instrumental in the determination of the false water thickness artefact and the correction of it. The length bar is 0.4 mm.

then determined from the corrected images, an example of which is shown in Fig. 8.

3. Results and discussion

In this section, the experimentally measured attenuation coefficient for liquid water is compared with the reference value from the NIST X-ray database. The improved accuracy of the water thickness measurements due to the movement correction technique is also discussed.

3.1. Attenuation coefficient measurement

The measured attenuation coefficient for liquid water at 20 keV, 0.657 cm^{-1}, is 23.3% lower than the value from the NIST database, 0.810 cm^{-1}. This expected result was caused by higher-than-expected intensities that resulted from the scattering effect and higher harmonics.

To explain the difference between the attenuation coefficients, consider the imaging sample [in Fig. 1(*a*)] as a quantity of liquid water with a uniform thickness of X_w in the direction of the traversing X-ray beam. I_0 is the incident beam intensity and I_{att} is the attenuated beam intensity. Thus, the liquid water thickness at 20 keV can be determined with equation (1):

$$X_w = \left(1/\mu_{w,NIST}\right) \ln(I_0/I_{att}), \quad (6)$$

where $\mu_{w,NIST}$ is the reference attenuation coefficient of water.

However, the measured intensity at the scintillator, I_m, consists of two other types of intensities in addition to I_{att}: the scattered intensity and the attenuated beam with energy levels higher than 20 keV (the higher harmonics). As a result, the reference attenuation coefficient at 20 keV, $\mu_{w,NIST}$, cannot be used to accurately determine the water thickness. Hence, the following equation was modified from equation (6) to calculate the water thickness based on the measured intensity at the scintillator:

$$X_w = \left(1/\mu_{w,c}\right) \ln(I_0/I_m), \quad (7)$$

where $\mu_{w,c}$ is the attenuation coefficient of liquid water with the consideration of scattering radiation and higher harmonics. Based on equations (6) and (7), the experimentally calibrated $\mu_{w,c}$ is expected to be lower than the reference $\mu_{w,NIST}$ because the ideal attenuated intensity, I_{att}, is lower than the measured intensity at the scintillator, I_m. If the reference value from NIST was directly applied, the water content would have been underestimated by 18.9%. As the water content (or equivalent saturation) directly influences the cell performance, the attenuation coefficient calibration is critical for imaging PEM fuel cell using synchrotron X-ray facilities (Kim & Lee, 2013).

3.2. Water thickness at the anode channel region

Fig. 9 illustrates the calculated water thickness values as a function of horizontal position along the *x* axis for the anode channel region (Region 1 of Fig. 8) before and after movement correction was applied. At each *x* position, the average water thickness was determined by averaging over all pixels in the *y* axis within Region 1 of Fig. 8. Before the movement correction, the calculated water thicknesses reached extreme values of −0.193 cm and 0.216 cm. After applying the movement correction technique, the range of calculated water thicknesses in this region significantly dropped to ±0.04 cm. After this movement correction technique, two local peaks of liquid water content were observed in the edge transition regions. The residual water thickness values visible in Fig. 9 in the case where the movement correction has been applied is thought to be due to two sources of error: water attenuation and image instability. Thin films of water were likely to form on the anode channel walls because the imposed RH of 100% may have facilitated water condensation.

There are some limitations to the correction technique that should be noted. The development of our technique was highly influenced by the specifications of the bipolar plate, the through-plane field of view, and the experimental operating conditions. Particularly, the sharp vertical and horizontal channel edges facilitated a reliable correlation between the artefact value and the distance moved. Additionally, the water-free anode was a critical prerequisite for the calibration. Any water signal at the anode channel edge region will affect

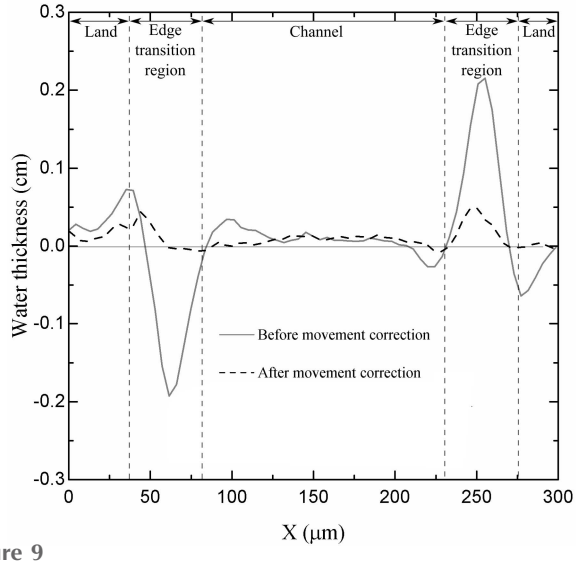

Figure 9
Calculated water thickness values as a function of horizontal position along the *x* axis for the anode channel region (Region 1 of Fig. 8) before and after the movement correction was applied.

the perceived artefact value. In future experiments, one could address these concerns by pre-emptively designing an additional channel-like structure on the bipolar plates that is outside the active area, yet within the field of view. The X-ray path that traverses these edges would be free of liquid water throughout the entire course of the experiment. Hence, the correction technique (calibration and application) could be performed even on experiments which involve the presence of liquid water in the anode. Furthermore, in order to apply this technique for both in-plane and through-plane imaging, the edges for movement correction should be designed such that the normal direction to their corresponding surfaces are perfectly perpendicular to the beam direction.

3.3. Water thickness at the cathode GDL region

An example single cathode channel/land region is shown in the inset of Fig. 10, which was cropped from Region 2 in Fig. 8. This figure includes the GDL below the channel and land of the cathode flow field. The water thicknesses for the highlighted area (white line whose height is a single pixel) are presented in this figure. Before the movement correction procedure was applied, significant negative water artefacts could be seen between x = 45 µm and 75 µm. The authors attributed this to the horizontal movement of the cell. Specifically, the GDL material was shifted out of this region in the wet-state image, so, during the image normalization, negative water thickness values were produced. After applying the image movement correction, the calculated water thickness profile became more homogeneous, and under the land region the largest measured water thickness was 0.30 cm.

The uneven distribution of water near the flow field observed in Fig. 10 can be attributed to the tendency for water to condense near the cold bipolar plate (Basu *et al.*, 2009; Manahan *et al.*, 2011; Owejan *et al.*, 2014; Turhan *et al.*, 2006; Yamada *et al.*, 2006). The raw image in Fig. 8 was obtained when the fuel cell was operating at a high current density of 2.5 A cm^{-2}. In the cathode GDL, saturated water vapour diffused from the cathode catalyst layer towards the cathode flow field. The catalyst layer was at a higher temperature than the flow field (60°C). Hence, water tended to condense in the GDL underneath the land region of the bipolar plate.

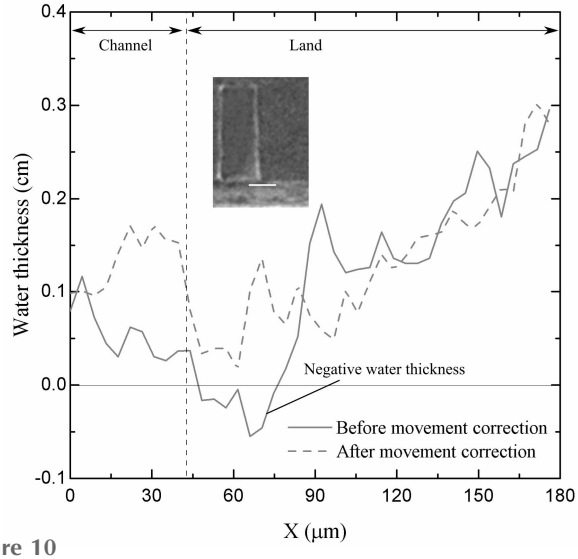

Figure 10
Calculated water thickness values along a selected region (white line) from Region 2 of Fig. 8, illustrating the impact of applying the movement correction.

4. Conclusion

In this work, we determined the primary cause of false water thicknesses measured during our synchrotron X-ray radiographic images of PEM fuel cells. We presented a procedure to obtain an experimental-specific attenuation coefficient for liquid water, and we presented our image-processing technique to correct for sample movement during synchrotron radiography.

A calibration experiment for the liquid water attenuation coefficient was conducted with a custom-made device which contained a water reservoir, which provided multiple parallel X-ray beam pathways, each with distinct pathway lengths for enabling a precise calibration for liquid water attenuation. The attenuation coefficient of liquid water was determined to be 0.657 $\pm$ 0.023 cm^{-1} with a confidence level of 90%. The difference between the reference and experimentally calibrated attenuation coefficient values was attributed to the X-ray scattering effect and higher harmonics present during our experiments. The determination and application of our attenuation coefficient prevented the underestimation of liquid water by 18.9%.

The false water thickness artefacts caused by sample movement was found to produce a liquid water thickness error of up to 0.93 cm. It was also demonstrated that the calculated water content in the GDL, with a height of 1 pixel, was significantly affected by the movement despite the misleading impression of a seemingly accurate global water distribution. With the newly proposed correction methods, the negative water thickness error was reduced to $\pm$0.04 cm, which has a magnitude comparable with that of the experimental background noise.

The sample movement correction has been found to be a crucial step needed before applying the Beer–Lambert law calculation. This work has provided valuable insight into the impact of microscale sample movement on false water thickness detection for PEM fuel cell researchers using synchrotron X-ray facilities, and this work also provides a useful tool for synchrotron researchers to address image movement and the scattering and higher harmonics that can lead to artefacts in a broader array of applications that may be the focus of X-ray imaging.

Acknowledgements

The authors would like to acknowledge the BMIT beamline team for the generous help at the Canadian Light Source, in Saskatoon, SK, Canada. The Thermofluids for Advanced Materials (TEAM) laboratory at the University of Toronto is gratefully acknowledged for their support and assistance.

Financial support from the Natural Sciences and Engineering Research Council of Canada (NSERC), the NSERC Collaborative Research and Training Experience (CREATE) Program in Distributed Generation for Remote Communities, the Canada Research Chairs Program, and the Ontario Ministry of Research and Innovation Early Researcher Award are gratefully acknowledged.

References

Alink, R., Haussmann, J., Markötter, H., Schwager, M., Manke, I. & Gerteisen, D. (2013). *J. Power Sources*, **233**, 358–368.
Antonacci, P., Chevalier, S., Lee, J., Ge, N., Yip, R., Hinebaugh, J., Tabuchi, Y., Kotaka, T. & Bazylak, A. (2016). *Electrochem. Acta*, **188**, 888–897.
Antonacci, P., Chevalier, S., Lee, J., Yip, R., Ge, N. & Bazylak, A. (2015). *Int. J. Hydrogen Energy*, **40**, 16494–16502.
Basu, S., Wang, C. Y. & Chen, K. S. (2009). *J. Electrochem. Soc.* **156**, B748–B756.
Büchi, F. N., Flückiger, R., Tehlar, D., Marone, F. & Stampanoni, M. (2008). *ECS Trans.* **16**, 587–592.
Chapman, D., Moulin, H. & Garrett, R. (1992). *Rev. Sci. Instrum.* **63**, 893–895.
Chevalier, S., Ge, N., Lee, J., Antonacci, P., Yip, R., George, M. G., Liu, H., Banerjee, R., Fazeli, M. & Bazylak, A. (2015). *Electrochem. Commun.* **59**, 16–19.
Eller, J., Roth, J., Marone, F., Stampanoni, M., Wokaun, A. & Büchi, F. N. (2014). *J. Power Sources*, **245**, 796–800.
Hartnig, C. & Manke, I. (2009). *Encyclopedia of Electrochemical Power Sources*, edited by C. K. Dyer, P. T. Moseley, Z. Ogumi, D. A. J. Rand & B. Scrosati, pp. 738–757. Amsterdam: Elsevier.
Hartnig, C., Manke, I., Kuhn, R., Kleinau, S., Goebbels, J. & Banhart, J. (2009). *J. Power Sources*, **188**, 468–474.
Haussmann, J., Markötter, H., Alink, R., Bauder, A., Dittmann, K., Manke, I. & Scholta, J. (2013). *J. Power Sources*, **239**, 611–622.
Hendee, W. R., Chaney, E. L. & Rossi, R. P. (1977). *Radiologic Physics, Equipment and Quality Control*, pp. 64–71. Chicago: Year Book Medical Publishers.
Hinebaugh, J., Challa, P. R. & Bazylak, A. (2012*b*). *J. Synchrotron Rad.* **19**, 994–1000.
Hinebaugh, J., Lee, J. & Bazylak, A. (2012*a*). *J. Electrochem. Soc.* **159**, F826–F830.
Hinebaugh, J., Lee, J., Mascarenhas, C. & Bazylak, A. (2015). *Electrochim. Acta*, **184**, 417–426.
Hrdý, J., Mikulík, P. & Oberta, P. (2011). *J. Synchrotron Rad.* **18**, 299–301.
Hubbell, J. H. & Seltzer, S. M. (2004). *Tables of X-ray Mass Attenuation Coefficients and Mass Energy-Absorption Coefficients*, (version 1.4), http://physics.nist.gov/xaamdi.
Hwang, G. S., Parkinson, D. Y., Kusoglu, A., MacDowell, A. A. & Weber, A. Z. (2013). *ACS Macro Lett.* **2**, 288–291.
Kalidindi, A., Taspinar, R., Litster, S. & Kumbur, E. (2013). *Int. J. Hydrogen Energy*, **38**, 9297–9309.
Kim, S. & Lee, S. (2013). *J. Power Sources*, **230**, 101–108.
Lee, J., Hinebaugh, J. & Bazylak, A. (2013). *J. Power Sources*, **227**, 123–130.
Lee, J., Yip, R., Antonacci, P., Ge, N., Kotaka, T., Tabuchi, Y. & Bazylak, A. (2015). *J. Electrochem. Soc.* **162**, F669–F676.
Lee, S., Kim, S., Park, G. & Kim, C. (2010). *Int. J. Hydrogen Energy*, **35**, 10457–10463.
Li, H., Tang, Y., Wang, Z., Shi, Z., Wu, S., Song, D., Zhang, J., Fatih, K., Zhang, J., Wang, H., Liu, Z., Abouatallah, R. & Mazza, A. (2008). *J. Power Sources*, **178**, 103–117.
Manahan, M. P., Hatzell, M. C., Kumbur, E. C. & Mench, M. M. (2011). *J. Power Sources*, **196**, 5573–5582.
Manke, I., Hartnig, C., Grünerbel, M., Lehnert, W., Kardjilov, N., Haibel, A., Hilger, A., Banhart, J. & Riesemeier, H. (2007). *Appl. Phys. Lett.* **90**, 174105.
Markötter, H., Alink, R., Haussmann, J., Dittmann, K., Arlt, T., Wieder, F., Tötzke, C., Klages, M., Reiter, C., Riesemeier, H., Scholta, J., Gerteisen, D., Banhart, J. & Manke, I. (2012). *Int. J. Hydrogen Energy*, **37**, 7757–7761.
Markötter, H., Dittmann, K., Haussmann, J., Alink, R., Gerteisen, D., Riesemeier, H., Scholta, J., Banhart, J. & Manke, I. (2015). *Electrochem. Commun.* **51**, 133–136.
Markötter, H., Haussmann, J., Alink, R., Tötzke, C., Arlt, T., Klages, M., Riesemeier, H., Scholta, J., Gerteisen, D., Banhart, J. & Manke, I. (2013). *Electrochem. Commun.* **34**, 22–24.
Neville, A. M. & Kennedy, J. B. (1964). *Basic Statistical Methods for Engineers and Scientists*, pp. 255–265. New York: Thomas Y. Crowell.
Owejan, J. P., Trabold, T. A. & Mench, M. M. (2014). *Int. J. Heat Mass Transfer*, **71**, 585–592.
Perng, S., Wu, H. & Wang, R. (2014). *Energy Convers. Manage.* **80**, 87–96.
Roth, J., Eller, J. & Büchi, F. N. (2012). *J. Electrochem. Soc.* **159**, F449–F455.
Schneider, A., Wieser, C., Roth, J. & Helfen, L. (2010). *J. Power Sources*, **195**, 6349–6355.
Sprawls, P. (1977). *The Physical Principles of Diagnostic Radiology*, pp. 101–117. Baltimore: University Park Press.
Swinehart, D. (1962). *J. Chem. Educ.* **39**, 333.
The Center for X-ray Optics (2009). *X-ray Interactions With Matter*, http://henke.lbl.gov/optical_constants.
Turhan, A., Heller, K., Brenizer, J. S. & Mench, M. M. (2006). *J. Power Sources*, **160**, 1195–1203.
Widenhorn, R., Blouke, M. M., Weber, A., Rest, A. & Bodegom, E. (2002). *Proc. SPIE*, **4669**, 193.
Wysokinski, T. W., Chapman, D., Adams, G., Renier, M., Suortti, P. & Thomlinson, W. (2007). *Nucl. Instrum. Methods Phys. Res. A*, **582**, 73–76.
Yamada, H., Hatanaka, T., Murata, H. & Morimoto, Y. (2006). *J. Electrochem. Soc.* **153**, A1748–A1754.